THERMAL STRUCTURE AND RADIUS EVOLUTION OF IRRADIATED GAS GIANT PLANETS

PHIL ARRAS AND LARS BILDSTEN

Kavli Institute for Theoretical Physics
Kohn Hall, University of California,
Santa Barbara, CA 93106; arras@kitp.ucsb.edu, bildsten@kitp.ucsb.edu

Draft version February 5, 2008

ABSTRACT

We consider the thermal structure and radii of strongly irradiated gas giant planets over a range in mass and irradiating flux. The cooling rate of the planet is sensitive to the surface boundary condition, which depends on the detailed manner in which starlight is absorbed and energy redistributed by fluid motion. We parametrize these effects by imposing an isothermal boundary condition $T \equiv T_{\rm deep}$ below the photosphere, and then constrain $T_{\rm deep}$ from the observed masses and radii. We compute the dependence of luminosity and core temperature on mass, $T_{\rm deep}$ and core entropy, finding that simple scalings apply over most of the relevant parameter space. These scalings yield analytic cooling models which exhibit power-law behavior in the observable age range $0.1 - 10$ Gyr, and are confirmed by time-dependent cooling calculations. We compare our model to the radii of observed transiting planets, and derive constraints on $T_{\rm deep}$. Only HD 209458 has a sufficiently accurate radius measurement that $T_{\rm deep}$ is tightly constrained; the lower error bar on the radii for other planets is consistent with no irradiation. More accurate radius and age measurements will allow for a determination of the correlation of $T_{\rm deep}$ with the equilibrium temperature, informing us about both the greenhouse effect and day-night asymmetries.

Subject headings: planetary systems–planets and satellites:general

1. INTRODUCTION

Following the discovery of the planet orbiting 51 Peg (Mayor & Queloz 1995; Marcy & Butler 1995), more than 160 planets have been found around nearby stars using precision Doppler spectroscopy. [1] Theories of planet formation now have the demanding task of explaining the existence of gas giants with semi-major axes one hundred times smaller than Jupiter, others with order unity orbital eccentricities, a detailed spectrum of (minimum) planet masses, and metallicity correlations with the parent star.

The discovery of transiting planets in the last five years (see Table 1) challenges not only theories for the origin of short-period gas giants, but also their structure and thermal evolution, spectrum, and interior fluid dynamics. Measurements of planetary mass, radius, and (stellar) age test cooling models which predict radius as a function of mass and age. The atmospheres of two planets have been directly observed. For HD 209458b, absorption lines (due to stellar photons passing through planet's atmosphere) have been found (Charbonneau et al. 2002; Vidal-Madjar et al. 2003, 2004), and the first detections of photons emitted by planets outside our solar system have been made for the thermal emission from HD 209458b (Deming et al. 2005) and TrES-1 (Charbonneau et al. 2005). These observations directly constrain the atmospheric structure, temperature profile and chemical composition near the photosphere.

Evolution of the short orbital period transiting exoplanets is significantly different than for Jupiter and Saturn due to proximity of the parent star (Guillot et al. 1996). Irradiation increases the photospheric temperature by nearly an order of magnitude relative to an isolated planet. Irradiation also decreases the cooling rate, and hence the rate of shrinkage, by altering the surface boundary condition (Burrows et al. 2000). This is immediately apparent in Table 1 as many transiting extra-solar giant planets (EGP's) have radii significantly larger than Jupiter. As short period planets are expected to be tidally synchronized (Guillot et al. 1996; Marcy et al. 1997), the strong day-night temperature contrast will drive winds to transport heat from the day to the night side (Showman & Guillot 2002). Hence the atmospheric temperature profile depends on a combination of detailed radiative transfer calculations for absorption of starlight, and hydrodynamics to model day-night winds and dissipation of wind kinetic energy. Lastly, tides raised on the planet by the parent star may significantly affect its thermal evolution (Bodenheimer et al. 2001; Showman & Guillot 2002). The free energy available by synchronizing the planet's spin or circularizing the orbit are comparable or larger than the thermal energy. Hence *if* the heat can be deposited sufficiently deep in the planet in less than a cooling timescale, the cooling can be slowed, or even reversed. However, it is uncertain if tides can deposit heat deep in the planet (Lubow et al. 1997; Ogilvie & Lin 2004; Wu 2004) .

Evolutionary models show that the cooling rate is quite sensitive to the uncertain surface boundary condition (Guillot & Showman 2002). This boundary condition has been implemented using various approximations. Full radiative transfer calculations (Barman et al. 2001; Hubeny et al. 2003) of *static* atmospheres include the stellar irradiation self-consistently, and determine the temperature structure for a given cooling flux from the deep interior. These calculations compute (rather than assume) the albedo, and determine the temperature rise due to absorption of starlight (the greenhouse effect). Such detailed radiative transfer solutions have

---

[1] For up to date catalogs, see http://exoplanets.org/ and http://obswww.unige.ch∼udry/planet/planet.html.

TABLE 1
TRANSITING EXTRASOLAR PLANETS

object	a(au)	$M_p(M_J)$	$R_p(R_J)$	$T_{eq}[K]$ [a]	$T_{deep}[K]$ [b]	Age (Gyr)	Reference
OGLE-TR-132	0.031	1.19 ± 0.13	1.13 ± 0.08	2100	≤ 2200	0–1.4	1
OGLE-TR-56	0.023	1.24 ± 0.13	1.25 ± 0.08	2100	$1000 - 3100$	3 ± 1	2,3,12
HD 209458	0.046	0.69 ± 0.05	$1.31^{+0.05}_{-0.05}$	1500	2200-2800	4–7	4,5
OGLE-TR-10	0.042	0.63 ± 0.14	1.14 ± 0.09	1500	≤ 2600	–	6,12
OGLE-TR-113	0.023	1.35 ± 0.22	$1.08^{+0.07}_{-0.05}$	1300	≤ 2100	–	7
TrES-1	0.039	0.73 ± 0.04	$1.08^{+0.05}_{-0.05}$	1200	≤ 1000	2.5 ± 1.5	5,8
OGLE-TR-111	0.047	0.52 ± 0.13	0.97 ± 0.06	1000	≤ 1200	–	9,12
HD 149026 [c]	0.042	0.36 ± 0.04	0.725 ± 0.05	1700		2.0 ± 0.8	10
HD 189733	0.031	1.15 ± 0.04	1.26 ± 0.03	1200	≤ 3200		11

REFERENCES. — (1) Moutou et al. (2004), (2) Torres et al. (2004), (3) Sasselov (2003), (4) Cody & Sasselov (2002), (5) Laughlin et al. (2005), (6) Konacki et al. (2005), (7) Bouchy et al. (2004), (8) Sozzetti et al. (2004), (9) Pont et al. (2004), (10) Sato et al. (2005),(11)Bouchy et al. (2005), (12) Santos et al. (2006)

[a]Here $T_{eq} \equiv T_*(R_*/2a)^{1/2}$. See the discussion following eq. (1).

[b]Allowed range of T_{deep} given range of mass, radius and age. If no age range given in the literature, we (arbitrarily) give the maximum value of T_{deep} for an age less than 10Gyr. However, given an accurate age range, the figures in § 8 can be used to obtain stronger constraints than given here.

[c]HD 149026's small radius clearly indicates a large core size or heavy element abundance. The present paper does not include heavy element cores, so we do not discuss HD 149026 further.

been incorporated as boundary conditions for some evolutionary calculations (Baraffe et al. 2003; Burrows et al. 2003). However, as day-night and equator-pole winds are not included, assumptions must be made about how the stellar flux is deposited over the surface of the planet (only day-side versus evenly over the entire surface, etc.) which directly affect the temperature profile. Other evolutionary calculations (e.g. Bodenheimer et al. 2003) solve the radiation diffusion equation and set the temperature at (infrared) optical depth 2/3 to be the equilibrium temperature, ignoring additional temperature increase due to absorption of starlight. Lastly, a number of groups (Showman & Guillot 2002; Cho et al. 2003; Burkert et al. 2005; Cooper & Showman 2005; Iro et al. 2005) are beginning to model the day-night winds on tidally locked, short orbital period planets, and the role of clouds Fortney et al. (2003) . As we stress here, the crucial parameter for the cooling rate is the temperature at the radiative-convective boundary, which is orders of magnitude deeper in pressure than the photosphere.

The plan of the paper is as follows. The uncertain surface boundary condition is discussed in § 2, motivating the surface isotherm used in our models. Details of cooling models and microphysical input are described in § 3. In § 4 we compute the dependence of the luminosity on planet mass, core entropy and irradiation. An analytic solution for the temperature profile in the radiative zone, and the position of the radiative-convective boundary are derived in § 5. These results are collected together in § 6 to derive an analytic cooling model which exhibits simple power-law dependence on time. The radii of irradiated gas giant planets are discussed in § 7, and the analytic formula for the radius given in eq. (32). We apply our models to the observed transiting planets and give constraints on the temperature of the deep surface isotherm in § 8. Our main conclusions are summarized in § 9.

2. SURFACE BOUNDARY CONDITION

The surface boundary condition we adopt is to set the temperature $T \equiv T_{deep}$ at a sufficiently large optical depth that the stellar light is fully absorbed, and the radiation diffusion approximation is valid. This choice of surface boundary condition has also recently been advocated by Iro et al. (2005), based on the results of time-dependent radiative models for the atmosphere of HD 209458b. We motivate our choice with a simple toy problem, and then discuss its relation to detailed radiative transfer solutions for the atmosphere.

The atmosphere is heated by absorption of starlight, and possibly dissipation of day-night winds and tidal flows. Let there be an energy deposition rate ε per unit volume in a radiative region of thickness Δz. Choose boundary conditions $T = 0$ at the top (for simplicity) and outward flux $F = 0$ at the base of the heated layer. The latter choice is required in steady state so that the temperature deeper in the atmosphere not increase in time. The flux generated in the layer, which exits the planet, is $F = \varepsilon \Delta z$, and the temperature of the deep atmosphere is $T_{deep} \sim (\tau F/\sigma)^{1/4}$, where $\tau = \kappa \rho \Delta z$ is the optical depth, ρ is the density and κ is the opacity. Hence an atmosphere subject to intense heating is expected to develop a deep isothermal region below the heated layer, the temperature determined primarily by the energy flux and depth of the layer, through τ. This estimate of the deep isotherm temperature is similar to that found for absorption of starlight for the proper choice of τ (Hubeny et al. 2003).

We now discuss the temperature profile for static atmospheres in more detail. In the absence of external irradiation, the photosphere of a planet will cool to a temperature $T_{cool} \sim (F_{cool}/\sigma)^{1/4} \sim 100$ K in a few Gyr's, where F_{cool} is the flux from the deep interior. A characteristic temperature at small optical depth for an irradiated

planet can be defined by balancing absorbed and emitted energy flux. For a star with mass M_*, radius R_* and effective temperature T_* a distance $a = (GM_* P_{\rm orb}^2/4\pi^2)^{1/3}$ away, this "equilibrium" temperature is

$$T_{\rm eq} \equiv T_*(R_*/2a)^{1/2}$$

$$\simeq 1400 \text{ K} \left(\frac{3 \text{ day}}{P_{\rm orb}}\right)^{1/3} \left(\frac{T_*}{6000 \text{ K}}\right) \left(\frac{R_*}{R_\odot}\right)^{1/2} \left(\frac{M_\odot}{M_*}\right)^{1/6} \tag{1}$$

an order of magnitude larger than for an isolated planet. Hence the surface boundary condition is drastically altered from the isolated case. In general, the irradiated boundary condition will cause the planet to cool slower (Burrows et al. 2000), as we discuss in detail. As significant horizontal temperature variation is expected above the photosphere, $T_{\rm eq}$ is an average temperature which gives the correct outgoing flux. Eq. (1) assumes zero reflection of the stellar photons, and should be multiplied by $(1-A)^{1/4}$ for nonzero Bond albedo A.

The (optical) incoming stellar photons not scattered back out of the planet are absorbed at the starlight's photosphere, typically at a pressure $\lesssim 10^6$ dyne cm^{-2}. Radiative balance implies an outgoing (infrared) flux $F \sim (T_{\rm eq}/T_{\rm cool})^4 F_{\rm cool} \sim 10^4 F_{\rm cool}$ generated by thermal emission. This large flux may lead to a significant increase in temperature above $T_{\rm eq}$ (the greenhouse effect, e.g. Hubeny et al. 2003). This situation continues to a depth at which the starlight is fully absorbed, at which point the temperature profile becomes isothermal. Hence, a semi-infinite atmosphere subject to external irradiation, and with no internal flux deep in the atmosphere, becomes isothermal at large optical depth. We label the temperature of this deep isotherm $T_{\rm deep}$. Now including the internal cooling flux $F_{\rm cool}$, the temperature will again rise toward the interior, the gradient eventually becoming large enough for convection to occur.

Since the cooling luminosity is generated in deep layers with sufficiently large optical depth that the stellar light is fully absorbed, the radiation diffusion approximation is valid there. Furthermore, we will show in § 5 that the temperature profile becomes isothermal within a pressure scale height of the radiative-convective boundary. Hence the problem of determining the cooling luminosity is insensitive to many of the details of the absorption of starlight. The only input needed from the full radiation transfer problem near the photosphere is the temperature of the deep isotherm, $T_{\rm deep}$. [2]

For tidally locked planets, the day side will be significantly hotter than the night side in static atmospheres with negligible day-night winds. A more uniform temperature distribution results if winds can carry heat from the day to the night side without suffering radiative losses (e.g. Iro et al. 2005). We will show that the cooling luminosity is determined in deep layers with thermal time $t_{\rm th} \gtrsim 10^3$ yr. While significant day-night temperature asymmetries may exist near the optical photosphere, winds moving at even a tiny fraction, $\sim 10^{-5}$, of the sound speed could deposit heat on the night side in

less than a thermal time at the depths where the cooling luminosity is determined. Hence we have a strong expectation of a near-spherically symmetric, isothermal temperature profile deep in the radiative layer.

3. NUMERICAL MODELS FOR THE INTERIOR

In the deep interior where the diffusion approximation is valid, we solve the mechanical and thermal structure equations (Landau & Lifshitz 1959)

$$\frac{dm}{dr} = 4\pi r^2 \rho, \tag{2}$$

$$\frac{dP}{dr} = -\frac{Gm\rho}{r^2}, \tag{3}$$

$$\frac{dT}{dr} = \frac{dP}{dr}\frac{T}{P}\nabla, \tag{4}$$

$$\frac{dl}{dr} = \frac{dm}{dr}\left(\varepsilon - T\frac{\partial S}{\partial t}\right), \tag{5}$$

for the interior mass m, pressure P, temperature T, and outward luminosity l, as a function of radius r. Here S is the entropy per gram, and $\nabla = d\ln T/d\ln P$ is the logarithmic temperature gradient. The energy generation ε is set to zero throughout this paper, as we study passively cooling planets. The subscript "cool" on the luminosity will be assumed for the rest of the paper. As the eddy turnover time is much shorter than the cooling time and convection is quite efficient, entropy is very nearly constant in space in the convection zone, but decreases in time due to cooling. Hence we treat $\partial S/\partial t$ as a constant in the convection zone. For numerical convenience, we use this same value of $\partial S/\partial t$ in the surface radiative zone. A negligible luminosity is generated there however, so this error does not affect our results. While the entropy equation (5) is valid on timescales longer than an eddy turnover time ($\sim$ yrs) in the convective core, the assumption of nearly spatially constant luminosity is only valid in the radiative envelope on timescales longer than the thermal time ($\sim 10^3$ yr) there. As this is much shorter than the global cooling time, we expect our numerical cooling models to be as accurate as a relaxation (Henyey-type) code.

The equation of state (EOS) from Saumon et al. (1995) (SCVH) is used with a mixture of 70% hydrogen and 30% helium, ignoring metals, and using the tables which smooth over the plasma phase transition. There are been several improvements to SCVH (Saumon et al. 1999; Fortney & Hubbard 2004) using recent laser shock- compression data and including the effects of helium phase separation, which change the radii at the few percent level. We use the solar composition "condensed" phase opacities from Allard et al. (2001), which includes the effects of grains in the equation of state, but ignores their opacity, as is appropriate if the grains have condensed out. Mixing length theory is used to calculated ∇ in convective regions, and radiative diffusion in radiative regions. The mixing length is set equal to the pressure scale height.

Two boundary conditions are needed at the surface. First, the surface temperature is set to $T_{\rm deep}$, the temperature of the deep isotherm discussed in § 2. The second boundary condition is that we specify the surface to be at the (arbitrarily chosen) pressure $P = 10^4$ dyne cm^{-2}. As the surface layer is isothermal, the contribution to

---

[2] We expect that the degree to which this layer is isothermal depends on the number of pressure scale heights separating the optical photosphere from the radiative-convective boundary. Larger irradiation and lower core entropy should make this layer more nearly isothermal.

the radius from near-surface layers is larger than for the radiative zero temperature profile, hence care is needed when comparing the radii computed here with previous work. As the radius is somewhat dependent on the problem at hand (optical photosphere versus infrared photosphere, corrections due to geometry in a transit, etc.) we have made this arbitrary choice of the surface for simplicity. The change in radius between pressures P_1 and P_2 is $\Delta R = \int_{P_1}^{P_2} d\ln P (k_b T/\mu m_p g) \simeq (k_b T/\mu m_p g) \ln(P_2/P_1)$. For example, the radius must be decreased by $\Delta R = -0.022 R_J$ for an outer boundary condition $P = 10^6$ dyne cm^{-2} for $T = 1000$ K and mean molecular weight $\mu = 2.43$ (70% molecular hydrogen and 30% neutral helium). We do not include a solid core in the present calculations.

We make a single model of a planet as follows. Planet mass M, core entropy S, and surface temperature $T_{\rm deep}$ are treated as fixed parameters. Assuming values for the planet's radius R, cooling luminosity $L = l(R)$, $\partial S/\partial t$, and central pressure P_c, we integrate outward from the center and inward from the surface. The four parameters are adjusted to make the integration variables (m, P, T, and l) continuous at a fitting radius. Given the subroutine to solve for a single model, evolving the planet in time is trivial. As we specify the core entropy S, and have solved for $\partial S/\partial t$, we compute the time it takes to cool from one entropy to the next.

4. IMPACT OF IRRADIATION ON HEAT LOSS

We now show the dependence of the cooling luminosity on the depth of the radiative-convective boundary, emphasizing the role of the opacity deep in the planet. Many of the luminosity dependences can be understood with purely local arguments, without the need to build a global planet model. Hence, qualitative statements can be made about cooling of EGP's under irradiation just given EOS and opacity tables. We make comparisons between the local arguments and the global numerical calculations as well.

The convective core is capable of transporting enormous luminosities through fluid motion. Hence it is the large thermal resistance of the outer radiative envelope that determines the cooling flux. For an opacity which increases inward from the surface, this resistance is largest at the base of the radiative layer, hence it is the radiative-convective boundary that determines the cooling flux. This boundary is moved to higher pressures by irradiation (Guillot et al. 1996).

The outward flux carried by radiative diffusion is

$$F = -\frac{16\sigma T^3}{3\kappa\rho}\frac{dT}{dr}, \qquad (6)$$

where κ is the Rosseland mean opacity. The maximum flux which can be carried by radiative diffusion is found using the adiabatic temperature gradient $dT/dr|_{\rm ad} = (\nabla_{\rm ad}T/P)(-Gm\rho/r^2)$, where $\nabla_{\rm ad} = \partial\ln T/\partial\ln P|_S$ ($= 2/7$ for an ideal gas with five degrees of freedom) is the adiabatic temperature gradient. Multiplying by $4\pi r^2$, the maximum luminosity per unit mass which can be carried by radiative diffusion at a local temperature T, pressure P, opacity $\kappa(T,P)$, and enclosed mass $m \simeq M$ is

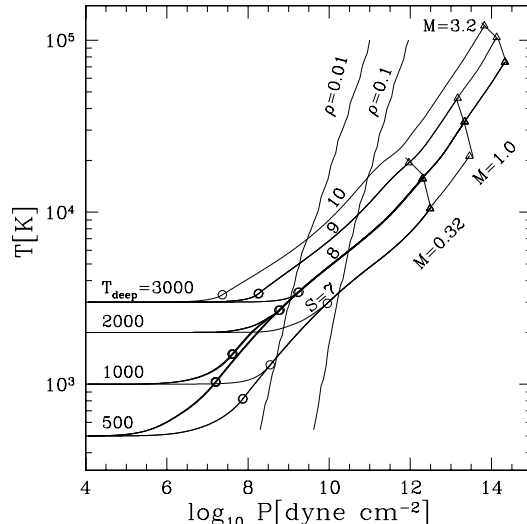$$\frac{L}{M} = \frac{64\pi G}{3}\frac{\sigma T^4}{\kappa P}\nabla_{\rm ad}. \qquad (7)$$

FIG. 1.— Run of temperature vs. pressure for numerical models with $T_{\rm deep} = 500, 1000, 2000, 3000$ K, $Sm_p/k_b = 7, 8, 9, 10$ and $M/M_J = 0.32, 1.0, 3.2$. Only the 19 curves in the age range $0.1 - 10$ Gyr are shown out of the total 48 curves. The circles show the position of the radiative-convective boundary. The triangles mark the center of the planet. Curves for different masses at the same S and $T_{\rm deep}$ nearly overlie each other. The two nearly vertical lines show contours of constant density $\rho = 0.01$ g cm^{-3} (left) and 0.1 g cm^{-3} (right).

Choosing an entropy S, the right hand side of eq. (7) can be evaluated along an adiabat out from the center, yielding the cooling flux for a specified temperature $T_{\rm rcb}$ at the radiative-convective boundary. Eq. (7) shows that the luminosity per unit mass depends solely on the entropy and irradiating flux, and that the luminosity is proportional to the planet's mass. [3]

Figure 1 shows the run of temperature versus pressure from numerical models for a range of M, S and $T_{\rm deep}$. Choosing S and $T_{\rm deep}$, the temperature profile must follow the adiabat deep in the planet and the isotherm near the surface. An even stronger statement can be made, however. The temperature profile over the entire planet from the center to the top of the deep isotherm depends only on S and $T_{\rm deep}$, and is independent of M (since eq. (11) and (12) depend only on $F/g \propto L/M$). Next, for a given irradiation flux (fixed $T_{\rm deep}$), the radiative-convective transition burrows deeper into the planet with time (decreasing S). Increasing the irradiation flux at fixed S also moves the radiative-convective region deeper into the planet.

Temperature changes in response to small changes in flux in optically thick regions occur on the thermal time, estimated from eq. (5) to be

$$t_{\rm th} = \frac{PC_pT}{gF} \simeq 10^4 \text{ yr}\left(\frac{P}{10^8 \text{ dyne cm}^{-2}}\right)\left(\frac{T}{10^3 \text{ K}}\right)$$
$$\left(\frac{10^3 \text{ cm s}^{-2}}{g}\right)\left(\frac{10^4 \text{ erg cm}^{-2} \text{ s}^{-1}}{F}\right). \qquad (8)$$

[3] It is commonly stated that the luminosity *decreases* with increasing mass. This is true at fixed core temperature, rather than fixed entropy. The derivatives can be related by $\partial\ln L/\partial\ln M|_{T_c} = \partial\ln L/\partial\ln M|_S + \partial\ln L/\partial S|_M \partial S/\partial\ln M|_{T_c}$. At fixed core temperature, entropy increases for decreasing mass (see Figure 6).
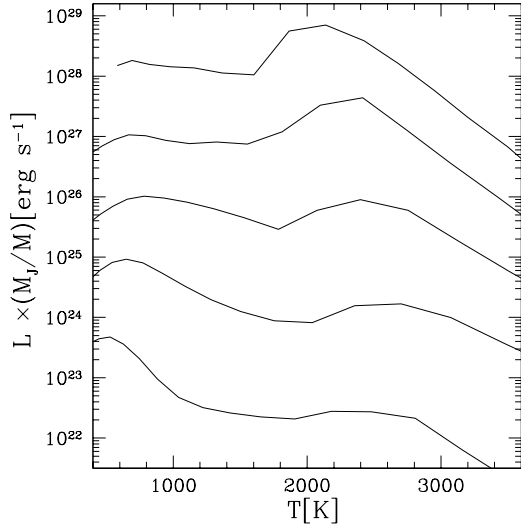
FIG. 2.— Maximum radiative luminosity (scaled to $M = 1M_J$; see eq. [7]) which can be carried by radiative diffusion vs. temperature along adiabats. The temperature T should be interpreted as $T_{\rm rcb}$, the temperature at the radiative-convective boundary. The five curves are for entropies $Sm_p/k_b = 6, ..., 10$, from bottom to top.
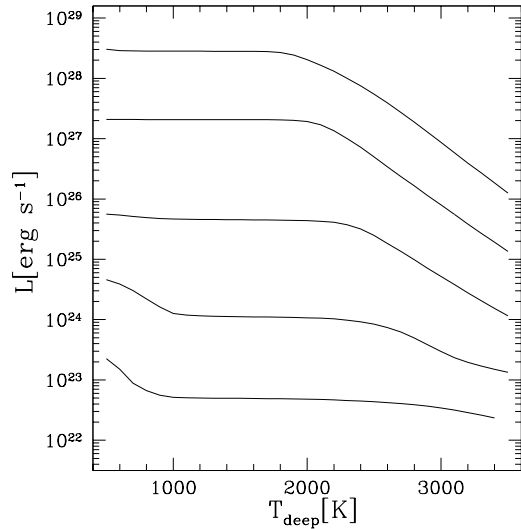

FIG. 3.— Luminosity vs. temperature of the deep isotherm from numerical calculation. Note that regions of positive slope in figure 2 correspond to zero slope here, implying the radiative-convective boundary jumps to a depth at which the slope is again negative. Calculation is for $M = M_J$, but can be extended to other masses using $L \propto M$. The lines represent core entropies $Sm_p/k_b = 6, ..., 10$ from bottom to top.

Here we have used typical numbers from Figure 1 for the radiative-convective boundary. Note that this estimate is much longer than the adjustment time near the optical photosphere ($\sim$ days, e.g. Iro et al. 2005), as the cooling flux is $\sim 10^4$ times smaller than the stellar flux, and the heat content increases $\propto TP$. As the thermal time at the radiative-convective boundary is so much longer than the horizontal sound travel time ($\sim$ days), we expect the day-night temperature asymmetry to be small there.

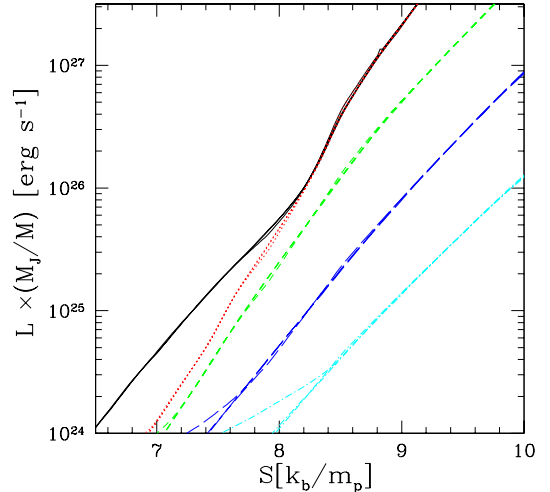Figures 2 and 3 show the local calculation of L/M

FIG. 4.— Luminosity per unit mass (scaled to 1 M_J) vs. entropy from numerical integrations. The lines correspond to surface isotherms $T_{\rm deep}[K]$ = 500 (solid black), 1000, (dotted red), 2500 (short dashed green), 3000 (long dashed blue), 3500 (dot short dash cyan). The lines for $T_{\rm deep}$ = 1500 and 2000 K overlie those for $T_{\rm deep}$ = 1000 K (see Figure 3). Three masses $M/M_J = 0.32, 1.0, 3.2$ are plotted, but closely overlie each other (except the largest masses at low entropies which are never reached) showing L/M is independent of mass at fixed S and $T_{\rm deep}$.

evaluated along adiabats, and the global calculation of L/M versus $T_{\rm deep}$, respectively. The x-axis in Figure 2 is the local temperature, which should be interpreted as $T_{\rm rcb}$, the temperature of the radiative-convective boundary. Care must be taken in Figure 2 in regions where $L(T)$ increases inward. As we show in § 6, $L(T)$ must *decrease* inward in order for convection to begin. Hence, if the chosen isotherm intersects a region of positive slope, such as the bump near $T = 2000 - 2500$ K, the convection zone actually begins at a deeper point at which the slope $L(T)$ is again negative. Such regions correspond to the flat parts of the curves in Figure 3. The result is that the luminosity generally decreases with irradiation temperature, or is roughly constant, but should not increase. This is the origin of the result found by previous investigators (Burrows et al. 2000) that irradiated planets cool slower. Comparison of Figures 2 and 3 show rough agreement in regions where $L(T)$ is decreasing, the main discrepancies due to the ratio $T_{\rm rcb}/T_{\rm deep}$ not being precisely a constant (see Figure 1).

Figure 4 shows luminosity versus core entropy for the numerical models. If $T_{\rm deep}$ is constant during the evolution, Figure 4 shows the change in luminosity as the planet cools. Comparison of lines with different $T_{\rm deep}$ clearly shows the monotonic decrease in luminosity as the irradiation temperature is increased. Aside from models with large mass ($M = 3.2M_J$) and irradiation temperature ($T_{\rm deep} = 3500$ K) at entropies so low ($S < 8k_b/m_p$) as to be unreachable in a Hubble time, the luminosity is proportional to the mass and the curves overlie each other.
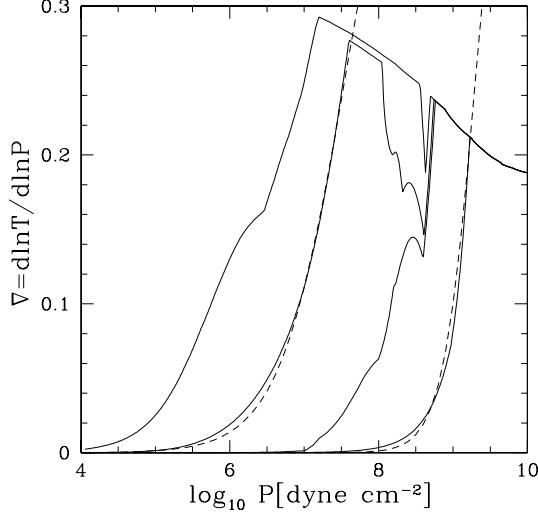
5. RADIATIVE-CONVECTIVE BOUNDARY

FIG. 5.— Solid lines show logarithmic temperature gradient ∇ as a function of pressure for models with $M = M_J$, $S = 8k_b/m_p$ and $T_{\rm deep}[K] = 500, 1000, 2000, 3000$ from left to right. The two dashed lines show the analytic formula in eq. (13) with parameters $(\nabla_\infty, a, P_{\rm deep}[{\rm dyne~cm}^{-2}]) = (0.5, 0.0, 3.5 \times 10^7)$ and $(0.5, 1.0, 2.0 \times 10^9)$. The upper envelope is set by the adiabatic gradient $\nabla_{\rm ad}$ in the convection zone. Note the appearance of a radiative window which causes the radiative-convective boundary to be at $P \simeq 10^{8.5}$ dyne cm^{-2} for a large range in $T_{\rm deep}$.

We now derive a simplified analytic model for the temperature profile at the transition from the surface radiative zone to the core convection zone. We relate $T_{\rm deep}$ to $T_{\rm rcb}$, the radiative-convective boundary temperature where the cooling luminosity is determined. The scalings derived here are used in § 6 to derive the scalings of the cooling luminosity.

We assume constant gravity g, ideal gas pressure $P = \rho k_b T / \mu m_p$ and power-law opacity [4] $\kappa \equiv \kappa_0 \rho^a T^b \equiv \kappa_1 P^a T^{b-a}$. In the radiative zone,

$$F = \frac{16\sigma T^3 g}{3\kappa} \frac{dT}{dP} = \frac{a+1}{4+a-b} \frac{16\sigma g}{3\kappa_1} \frac{dT^{4+a-b}}{dP^{a+1}}. \quad (9)$$

When integrating this equation, it's essential to retain the constant of integration. Defining the temperature gradient for a radiative zero solution $\nabla_\infty = (a+1)/(4+a-b)$, we find

$$T^{4+a-b} = {\rm constant} + \nabla_\infty^{-1} \left(\frac{3\kappa_1 F}{16\sigma g} \right) P^{a+1}. \quad (10)$$

At small pressure, $T \simeq T_{\rm deep}$, so we write the temperature profile as

$$T = T_{\rm deep} \left[1 + (P/P_{\rm deep})^{a+1} \right]^{1/(4+a-b)}, \quad (11)$$

which becomes isothermal below the pressure

$$P_{\rm deep} = \left(\nabla_\infty \frac{16\sigma g T_{\rm deep}^{4+a-b}}{3\kappa_1 F} \right)^{1/(a+1)}. \quad (12)$$

[4] Significant features in the opacity may be treated as broken power-laws.

The logarithmic temperature gradient is then

$$\nabla = \nabla_\infty \frac{(P/P_{\rm deep})^{a+1}}{1 + (P/P_{\rm deep})^{a+1}}, \quad (13)$$

which decreases sharply over a pressure scale height. A plot of ∇ versus P is shown in Figure 5 for several values of $T_{\rm deep}$. The upper envelope of the curves is set by the adiabatic gradient in the convection zone. Increasing $T_{\rm deep}$ moves the boundary inward along the adiabat, $P_{\rm deep} \propto T_{\rm deep}^{1/\nabla_{\rm ad}}$, aside from regions where the opacity changes irregularly. Eq. (13) agrees well with the numerical integrations in regions where the opacity is smooth.

To solve for the transition from radiative to convective zone, we set $\nabla = \nabla_{\rm ad}$. As $a + 1 > 0$, one must have the inequality $\nabla_\infty \geq \nabla_{\rm ad}$ for a convection zone to exist. We find the temperature and pressure at the boundary are

$$T_{\rm rcb} = T_{\rm deep} \left(\frac{\nabla_\infty}{\nabla_\infty - \nabla_{\rm ad}} \right)^{1/(4+a-b)}$$

$$P_{\rm rcb} = P_{\rm deep} \left(\frac{\nabla_{\rm ad}}{\nabla_\infty - \nabla_{\rm ad}} \right)^{1/(a+1)}, \quad (14)$$

so they differ by a factor of order unity from $T_{\rm deep}$ and $P_{\rm deep}$ unless $|\nabla_{\rm ad} - \nabla_\infty| \ll \nabla_\infty$. The decrease of $\nabla_{\rm ad}$ at large pressures seen in Figure 5 makes the ratio $T_{\rm rcb}/T_{\rm deep}$ closer to unity for large $T_{\rm deep}$ and P, as seen in Figure 1. Also note that at fixed S and $T_{\rm deep}$, $T_{\rm rcb}$ is largely independent of mass.

6. ANALYTIC COOLING MODEL

In § 4 we found that the luminosity scales with core entropy and irradiating flux over much of the relevant parameter space. Here we show that the core temperature also scales simply with mass and entropy when sufficiently degenerate. As a consequence, we derive an analytic model in which entropy has a simple power-law time dependence at late times. We compare the power-law model against numerical time integrations.

The scaling of luminosity with $T_{\rm deep}$ and S can be found by substituting $P(T, S)$ into eq. (7). Using the thermodynamic relation

$$\frac{dS}{C_p} = \frac{dT}{T} - \nabla_{\rm ad} \frac{dP}{P}, \quad (15)$$

and expanding about a reference point $T_{\rm ref}$, $P_{\rm ref}$ and $S_{\rm ref}$, the adiabat is

$$P \simeq P_{\rm ref} \left(\frac{T}{T_{\rm ref}} \right)^{1/\nabla_{\rm ad}} \exp\left(-\frac{\Delta S}{C_p \nabla_{\rm ad}} \right), \quad (16)$$

where $\Delta S = S - S_{\rm ref}$, and we approximate $\nabla_{\rm ad}$ and C_p as constants. For an ideal gas, $C_p \nabla_{\rm ad} = k_b/\mu m_p$, but particle interactions and molecular dissociation reduce $C_p \nabla_{\rm ad}$ below the ideal value. Inserting eq. (16), (14), and the power-law form of the opacity into eq. (7), we find

$$L \simeq L_{\rm ref} \left(\frac{T_{\rm deep}}{T_{\rm ref}} \right)^{-\alpha} \exp\left[\beta \frac{(S - S_{\rm ref})}{k_b/m_p} \right] \quad (17)$$

where the exponents are (Figures 3 and 4)

$$\alpha \simeq (4 + a - b) \left(\frac{\nabla_\infty}{\nabla_{\rm ad}} - 1 \right) \simeq 0.0 - 10.0,$$

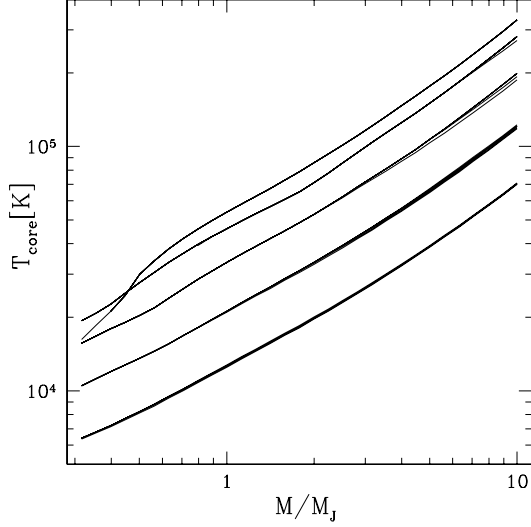$$\beta \simeq (a+1) \frac{k_b/m_p}{C_p \nabla_{\rm ad}} \simeq 2.5 - 3.5. \quad (18)$$

FIG. 6.— Core temperature vs. mass. The five groups of lines show entropies $Sm_p/k_b = 6, ..., 10$ from bottom to top. Each group contains surface isotherms $T_{\rm deep}[K] = 500, ..., 3500$, inducing larger spread for small entropy.
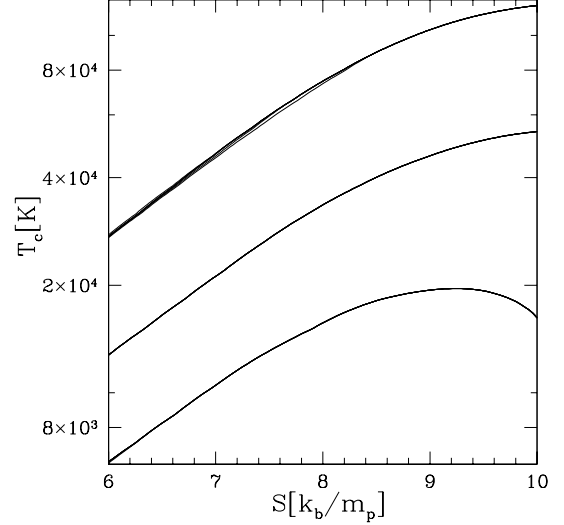

FIG. 7.— Core temperature vs. entropy. The three distinct lines are the masses $M/M_J = 0.32, 1.0, 3.2$ from bottom to top. For each mass, the irradiation temperatures $T_{\rm deep}[K] = 500, ..., 3500$ are plotted, but there is so little dependence on $T_{\rm deep}$ that the curves are indistinguishable.

Examination of the exponent α shows that irradiation slows the cooling, i.e. luminosity decreases as $T_{\rm deep}$ increases. The condition $\nabla_\infty > \nabla_{\rm ad}$ is required for a core convection zone to exist, hence $\alpha \geq 0$. Evaluation of α depends on the detailed density and temperature dependence of the opacity, which can be found in Figure 2. Features of note are the positive slope near $2000-3000$ K at which point α become small, and also the steep decrease for $T_{\rm rcb} \geq 3000$ K.

The exponent β can be estimated for an ideal gas (solar mixture, molecular hydrogen and neutral helium) and density independent opacity to be $\beta \simeq \mu \sim 2.4$. This ideal limit is expected for small $T_{\rm deep}$ and hence low density. As $T_{\rm deep}$ is increased, molecular interactions make the gas less ideal, reducing the value of $C_p \nabla_{\rm ad}$ and increasing β. This qualitative trend may be seen in Figure 4.

The core temperature increases during the initial contraction phase when the core is non-degenerate. A maximum is reached when $k_b T_c \simeq E_F$, the Fermi energy, and subsequently T_c decreases as entropy decreases. In this degenerate phase, the core temperature depends mainly on mass and entropy, with only a weak dependence on irradiation. Figure 6 shows core temperature versus mass for four adiabats and a range of irradiation temperatures. The dependence on $T_{\rm deep}$ gives only a slight broadening of each adiabat. The dependence on mass is quite simple when sufficiently degenerate. Figure 7 shows the dependence of core temperature on entropy for a range of masses and irradiation temperatures, showing a simple exponential dependence at low entropy. For the degenerate phase we write T_c in the form (see Figure 6)

$$T_c(M, S) = T_{c,{\rm ref}} \left(\frac{M}{M_{\rm ref}} \right)^\gamma \exp \left[\delta \frac{(S - S_{\rm ref})}{k_b/m_p} \right]. \quad (19)$$

Using hydrostatic balance $P \propto M^2/R^4$, and parameterizing $R \propto M^\lambda$, we estimate the exponents to be

$$\gamma \simeq \nabla_{\rm ad}(2 - 4\lambda) \simeq 0.6 - 0.7$$

$$\delta \simeq k_b/C_p m_p \simeq 0.5. \quad (20)$$

Next we solve for the change in core entropy with time for the analytic model. We treat $T_{\rm deep}$ and M as constants during the evolution. The entropy equation integrated over the convective core gives

$$\frac{\partial S}{\partial t} = -\frac{L/M}{f T_c}, \quad (21)$$

where $f = \int (dm/M)(T/T_c) \simeq 0.6 - 0.7$ and we have treated $\partial S/\partial t$ as constant in space. Plugging eq. (19) and (17) into eq. (21), we find the following solution for the entropy with time

$$\exp \left[\frac{S - S_{\rm ref}}{k_b/m_p} \right] = \left(1 + \frac{t}{t_{\rm S}} \right)^{-1/(\beta - \delta)}, \quad (22)$$

where the characteristic cooling time is

$$t_{\rm S}(M, T_{\rm deep})$$
$$= \left(\frac{f}{\beta - \delta} \right) \left(\frac{k_b T_c/m_p}{L/M} \right)_{\rm ref} \left(\frac{T_{\rm deep}}{T_{\rm deep,ref}} \right)^\alpha \left(\frac{M}{M_{\rm ref}} \right)^\gamma \quad (23)$$

This solution has a number of notable features:

(1) The fiducial evolution time, $M k_b T_c/m_p L$, is just the *initial* time to radiate away the core's thermal energy.

(2) At late times, $t \geq t_S$, the solution is a power-law in time. As the initial cooling time is very short, the power-law occurs for most of the planet's lifetime.

(3) The exponent of the power-law involves the change of luminosity and core temperature with respect to entropy.

(4) Evolution timescale is slowed for large irradiation or large planet mass. The dependence on
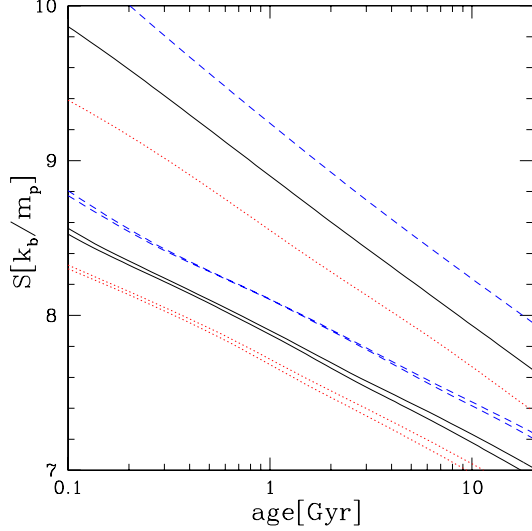
FIG. 8.— Core entropy vs. age for a planet mass $M/M_J = 0.32$ (dotted red), 1.0 (solid black), and 3.2 (dashed blue). For each mass, surface isotherms $T_{\rm deep}[K] = 1000, 2000, 3000$ are shown from bottom to top. Luminosity is independent of $T_{\rm deep}$ for $T_{\rm deep} = 1000 - 2000$ K, hence the curves nearly overlie each other (see Figure 3).
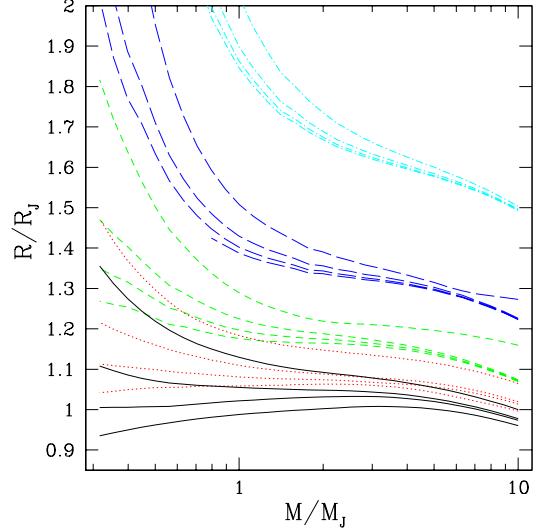

FIG. 9.— Radius vs. mass curves for different core entropy and irradiation. Each group of lines with a different color and line style denote different entropies. Solid black, dotted red, and short-dashed green, long dashed blue and dot-dashed cyan lines represent entropies $Sm_p/k_b = 6, ..., 10$. Each group of lines represents deep isotherms $T_{\rm deep} = 500, 1500, 2500, 3500$ K, from bottom to top.

planet mass comes purely from the dependence of T_c on planet mass (at fixed entropy). The dependence on irradiation is primarily through the luminosity.

Figure 8 shows entropy versus time for a range of mass and irradiation. Note the large spread in S at a given age. For low irradiation, $S \simeq 6 - 8k_b/m_p$ in the age range $1 - 10$ Gyr, while S can be as high as $\simeq 10k_b/m_p$ for $T_{\rm deep} = 3500$ K. While the range of $T_{\rm deep}$ shown here gives fairly good power-laws, we note that at $T_{\rm deep} < 500$ K there is a break occurring at $\simeq 1$ Gyr, due to the increase in luminosity seen in Figure 4 below $S = 8k_b/m_p$.

While we have used the SCVH EOS and Allard et.al.(2001) opacities for numerical estimates, the analytic solution makes it particularly clear which quantities need by evaluated for a given opacity table and EOS. The luminosity is sensitive only to the local conditions at the radiative-convective boundary, while the core temperature involves building static (i.e. not time-dependent) models.

7. RADIUS EVOLUTION

Planets are initially nondegenerate in their core, and undergo rapid contraction until the core is degenerate. If $T_{\rm eff}$ is constant during the contraction, the energy equation $d/dt(-3GM^2/7R) = -4\pi R^2\sigma T_{\rm eff}^4$ is solved to find the change in radius with time (see, e.g. Bildsten et al. 1997)

$$R(t) \simeq 8\ R_J\ \left(\frac{M}{M_J}\right)^{2/3}\left(\frac{300\ {\rm K}}{T_{\rm eff}}\right)^{4/3}\left(\frac{1\ {\rm Myr}}{t}\right)^{1/3} \quad (24)$$

The core temperature $T_c \simeq GM\mu m_p/Rk_b \propto t^{1/3}$ is increasing during the non-degenerate phase, and reaches a maximum when $k_bT \simeq E_F$. For an ideal gas, k_bT/E_F is a function only of entropy, so that the maximum temperature would occur at the same entropy for all planet

masses. Coulomb interactions suppress the value of $\nabla_{\rm ad}$ below 2/5, so that if $T_c \propto M^{4/3}$ and $P_c \propto M^{10/3}$, the entropy at maximum temperature will increase a bit with mass. This can be seen in Figure 7, as the two higher masses have maxima at higher entropy (off the plot) than the lowest mass.

Once degeneracy sets in, the radius is primarily determined in the degenerate core of the planet, although as irradiation is increased the contribution from the outer envelope becomes larger due to the increased scale height. This is clarified by writing the radius as an integral over pressure

$$r(P) = \int_P^{P_c} d\ln P\left(\frac{P}{\rho g}\right). \quad (25)$$

In the degenerate core, $P/\rho \propto E_F$ while in the nondegenerate envelope $P/\rho \propto k_bT$. The contribution from the core is larger when $E_F \gg k_bT$ unless the number of pressure scale heights in the envelope is much larger than the core.

The equation of state in the core for $M < M_J$ is complicated by strong Coulomb interactions. For illustrative purposes, an approximate equation of state including the leading order contributions from Coulomb interactions as well as ideal ion pressure is

$$P = n_e\left(\frac{2}{5}E_F - \frac{3}{10}\frac{Z^2e^2}{a_i}\right) + \frac{\rho k_bT}{\mu_i m_p}, \quad (26)$$

where $a_i = (4\pi\rho/\mu_i m_p)^{1/3}$ is the mean ion spacing and $\mu_i m_p$ is the mean ion mass. The energy scales relevant for the core are $E_F = (\hbar^2/2m_e)(3\pi^2\rho/\mu_e m_p)^{2/3} \simeq 26$ eV$(\rho\mu_e^{-1}{\rm g\ cm}^{-3})^{2/3}$, $k_bT \simeq 0.9$ eV$(T/10^4\ {\rm K})$, and $E_{\rm coul} = Z^2e^2/a_i \simeq 20$ eV$Z^2(\rho\mu_i{\rm g\ cm}^{-3})^{1/3}$ is the Coulomb interaction energy between a nucleus and uniform electron cloud. Ignoring the ion pressure term, the density at zero pressure is $\rho_{\rm zp} \simeq 0.2\mu_e Z^2{\rm g\ cm}^{-3}$. As
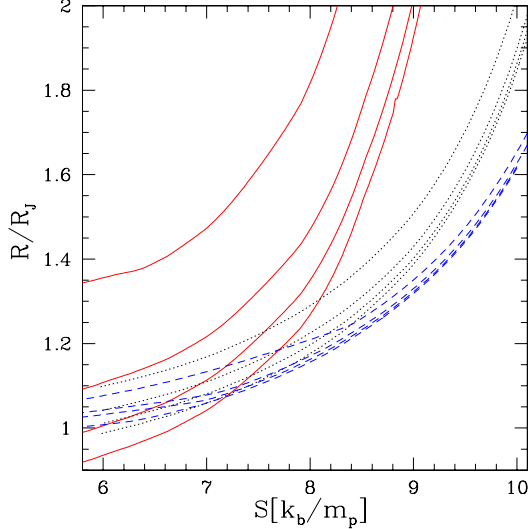
FIG. 10.— Radius vs. core entropy for different masses and irradiation. Solid red, dotted black, and dashed blue lines represent masses $M/M_J = 0.32, 1.0, 3.2$. Each group of lines represents $T_{\rm deep} = 500, 1500, 2500, 3500$ K, from bottom to top.

FIG. 11.— Comparison of computed fractional radius $(R(S) - R_0)/R_0$ (solid line) to fitting formula $R(S) = R_0 + \delta R_S e^{\eta m_p S/k_b}$ (dashed line) for a $M = 1$ M_J planet with $T_{\rm deep} = 1000$ K.

the central density in Jupiter mass objects is near $\rho_{\rm zp}$, Coulomb interactions (and further the tendency to form bound states) stiffen the EOS, and are important in determining the radius.

Figure 9 shows mass versus radius for a range of core entropy and irradiation. The effects of irradiation are seen to be most severe at low mass and low entropy, since $T_{\rm deep}$ is becoming a significant fraction of the core temperature. At $M \simeq M_J/2$ and low entropy, the range of irradiation temperatures shown here can change the radius by as much as 50%. Radii for fully adiabatic planets (not shown here) agree well with the $T_{\rm deep} = 500$ K lines.

Figure 10 shows radius versus entropy for a range of masses and irradiation temperature. At late times in the evolution when the entropy is small, the radius is converging to some constant value which depends on *both* M and $T_{\rm deep}$. If the planet were allowed to cool under a constant irradiation field indefinitely, it would approach an isothermal state (Hubbard 1977) at $T = T_{\rm deep}$ with a radius [5] $R = R_0$. Although in practice planets will never reach this isothermal state, it is the *minimum* radius to which the planet is evolving. Furthermore, it is the *deviation* around the isothermal radius, $\delta R = R - R_0$ which is changing with age. As we now show, δR has a particularly simple behavior with time over the entire observable range $\delta R \leq R$.

To motivate the following numerical calculations, we first discuss the change in radius for a fluid element in mass shell m as the entropy is changed. The radius of a mass shell in the convection zone can be written

$$r^3(m, S) = \frac{3}{4\pi} \int_0^m \frac{dm'}{\rho(m', S)}, \qquad (27)$$

hence for fixed interior mass the change in radius with respect to entropy is

$$\frac{\partial r}{\partial S} = -\frac{1}{4\pi r^2} \int_0^m \frac{dm'}{\rho(m', S)} \frac{\partial \rho(m', S)}{\partial S} \rfloor_{m'}. \qquad (28)$$

Given an equation of state $\rho(P, S)$, and switching to radius as the integration variable, we find

$$\frac{\partial r}{\partial S} = -\frac{1}{r^2} \int_0^r r'^2 dr' \left(\frac{1}{C_p} \frac{\partial \ln \rho}{\partial \ln T} \rfloor_P + \Gamma_1^{-1} \frac{\partial \ln P}{\partial S} \rfloor_m \right) (29)$$

where eq. (15) has been used. The second term in eq. (29) mainly corresponds to a uniform shift in pressure in the core, due to the radius changing. Near the surface this term must go to zero since pressure is proportional to external mass, which is fixed. Consequently, the first term is most important. From eq. (26), the volume expansion term is $\partial \ln \rho/\partial \ln T|_P \propto k_b T/E_F$, with a significant correction due to Coulomb interactions which acts to increase the expansion since the electron pressure is effectively lowered. Hence the change in radius in the core is proportional [6] to T_c. As T_c depends exponentially on the entropy (eq. [19]), the contribution to the radius from the degenerate core depends exponentially on entropy. In the nondegenerate envelope, $\partial \ln \rho/\partial \ln T|_P \simeq -1$. Plugging this result into eq. (29) implies that the change in radius due to the nondegenerate envelope scales linearly with entropy. As a consequence, it is less important than the exponential dependence from the core.

A suite of evolutionary calculations has been done for $M/M_J = 0.32, 1.0, 3.2$ and $T_{\rm deep}[K] = 500, 1000, ..., 3500$ starting from high entropy and evolved to ages greater than 15 Gyr. Given the run of $R(S)$, we fit a function

$$R(S) = R_0 + \delta R_0 \exp(\eta m_p S/k_b) \qquad (30)$$

---

[5] In principle, R_0 can be calculated by integrating the structure equations for a given EOS. In practice, such low temperatures and high densities are not covered by the SCVH EOS. In this paper, we compute the isothermal radius by fitting evolutionary curves of radius versus entropy, defining R_0 by extrapolating to the small entropy limit.
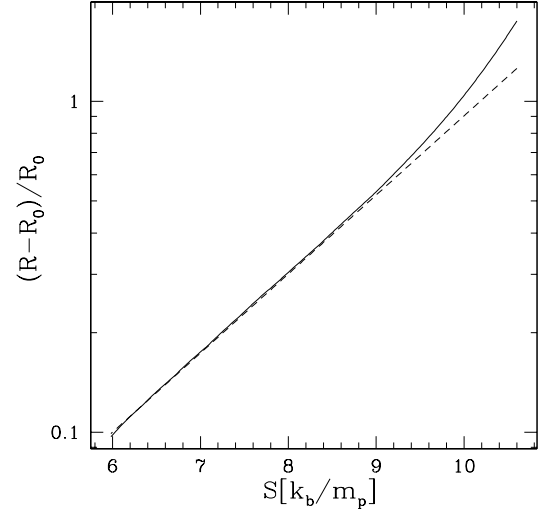
[6] Eq. (26) has ignored contributions to the Coulomb correction which depend on temperature, and do not scale linearly with temperature. Using the EOS in Potekhin & Chabrier (2000), we find the contribution of these terms to the volume expansion seems to be somewhat smaller than the ideal ion pressure.
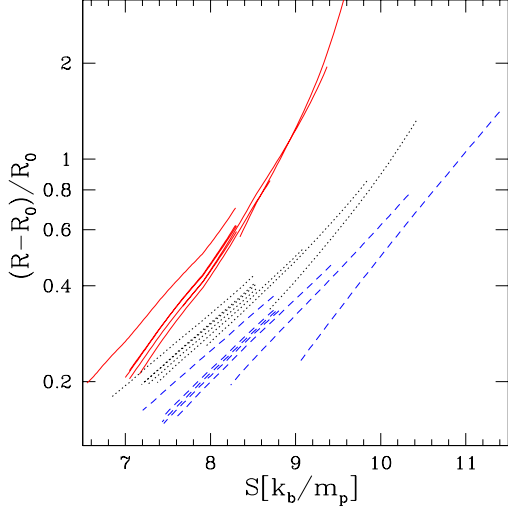
Fig. 12.— Fractional deviation in radius vs. core entropy for different masses and irradiation. This curves give a sense of how much the radius changes during evolution. Solid red, dotted black, and dashed blue lines represent masses $M/M_J = 0.5, 1.0, 1.5$. Each group of lines represents $T_{\rm deep} = 500, 1000, ..., 3500$ K, from left to right. Only ages in the range 0.1 to 10 Gyr are shown for each curve.

TABLE 2
PARAMETERS FOR THE FITTING FUNCTION $R(t)$ IN EQ. (32).

| M/M_J	$T_{\rm deep}[K]$	$\eta/(\beta-\delta)$	R_0/R_J	$\delta R_1/R_J$
0.316	500	0.31	0.836	0.308
0.316	1000	0.25	0.881	0.330
0.316	1500	0.23	0.905	0.359
0.316	2000	0.23	0.952	0.361
0.316	2500	0.32	1.05	0.401
0.316	3000	0.43	1.15	0.867
0.316	3500	0.50	1.30	2.49
1.00	500	0.16	0.825	0.320
1.00	1000	0.16	0.894	0.273
1.00	1500	0.15	0.902	0.280
1.00	2000	0.16	0.930	0.266
1.00	2500	0.24	0.992	0.264
1.00	3000	0.25	0.993	0.439
1.00	3500	0.35	1.09	0.727
3.16	500	0.20	0.915	0.243
3.16	1000	0.16	0.934	0.238
3.16	1500	0.17	0.947	0.227
3.16	2000	0.18	0.962	0.217
3.16	2500	0.26	0.994	0.239
3.16	3000	0.30	1.02	0.379
3.16	3500	0.41	1.10	0.673
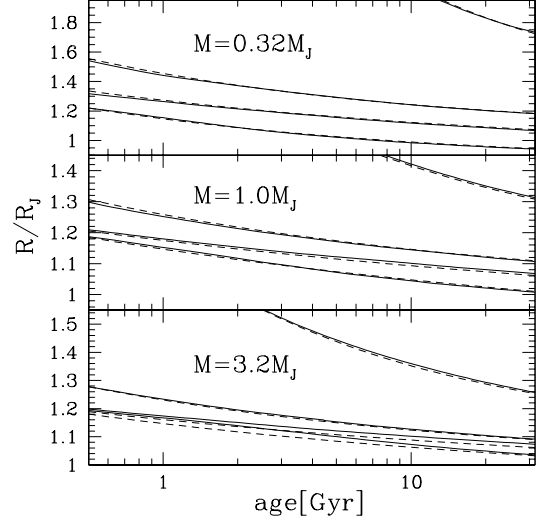
Fig. 13.— Radius vs. age for $M/M_J = 0.32, 1.0, 3.2$ and $T_{\rm deep} = 500, 1500, 2500, 3500$ K from bottom to top within each panel. Solid lines show the numerical evolutions, while dashed lines show the fitting formula in eq. (32).

to determine the isothermal radius R_0, coefficient δR_0, and exponent η. The coefficients R_0, δR_0 and η depend on M and $T_{\rm deep}$. The small entropy points were more heavily weighted to force the fit to agree there. The weighting was adjusted until the fit agreed for as large a region in S as possible (for the plots here we used weighting $\propto R^{10}$.) A comparison of the fit against the data for one example is given in Figure 11. The agreement is good at small entropies, and gets worse for large entropy as degeneracy is lifted. We find good agreement between $\eta \sim 0.5 - 0.7$ and δ from eq. (19), as expected if $\delta R \propto T_c$.

The deviation of the radius about the isothermal value is plotted for all runs over the age range $0.1 - 10$ Gyr in Figure 12. Recall that R_0 is different for each line. Note that each line is approximately a power-law, even to $\delta R/R_0 \simeq 1$, where the degenerate approximation breaks down. Hence the fitting formula often works better than naively expected.

We now combine the power-law cooling result in eq. (22) and (23) with the fit for the radius in eq. (30) to find

$$R(t) = R_0 + \delta R_0 \exp(\eta m_p S_{\rm ref}/k_b) \left(1 + \frac{t}{t_{\rm S}}\right)^{-\eta/(\beta-\delta)} \quad (31)$$

At late times $t \gg t_S$, the deviation in radius from the isothermal value is a power-law in time. In order to provide useful fits to our evolutionary tracks, we parametrize this late time power-law as

$$R(t) = R_0 + \delta R_1 \left(\frac{1 \text{ Gyr}}{t}\right)^{\eta/(\beta-\delta)}, \quad (32)$$

where R_0 is again the isothermal radius and $\delta R_1 = \delta R_0 \exp(\eta m_p S_{\rm ref}/k_b)(t_{\rm S}/1 \text{ Gyr})^{\eta/(\beta-\delta)}$ is the deviation at an age of 1 Gyr. We fit tracks of $R(t)$ to find the coefficients R_0, δR_1 and $\eta/(\beta-\delta)$ in the same way as the fits for $R(S)$ in eq. (30). The coefficients are given

in Table 2. Comparison between the numerical evolutionary tracks for $R(t)$ and the analytic fit in eq. (32) are given in Figure 13. The agreement is generally very good.

Approximate values and scalings of the coefficients in Table 2 can be understood as follows. The expected power-law index $\eta/(\beta-\delta) \simeq 0.6/3.0 = 0.20$ agrees well with the temperature range $T_{\rm deep} = 1000 - 2000$ K where L is independent of $T_{\rm deep}$. At large irradiation, Figure 12 shows η increases and Figure 4 shows that β decreases, explaining the increase in $\eta/(\beta-\delta)$. Since $\delta R_1 \propto t_S^{\eta/(\beta-\delta)} \propto T_{\rm deep}^{\alpha\eta/(\beta-\delta)}$, regions of constant (decreasing) slope in Figure 3 correspond to δR_1 being con-
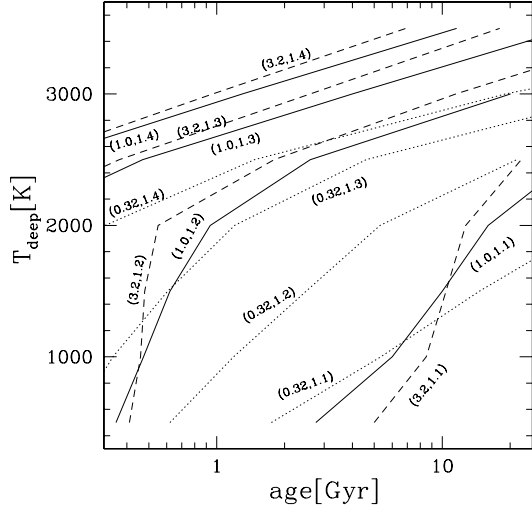
FIG. 14.— $T_{\rm deep}$ vs. age for planets with a given M and R. Shown are lines of constant radius for a given mass, labeled by $(M/M_J, R/R_J)$. At a given age, this plot shows the value of $T_{\rm deep}$ required to explain a certain mass and radius. There is significant degeneracy between $T_{\rm deep}$ and age.
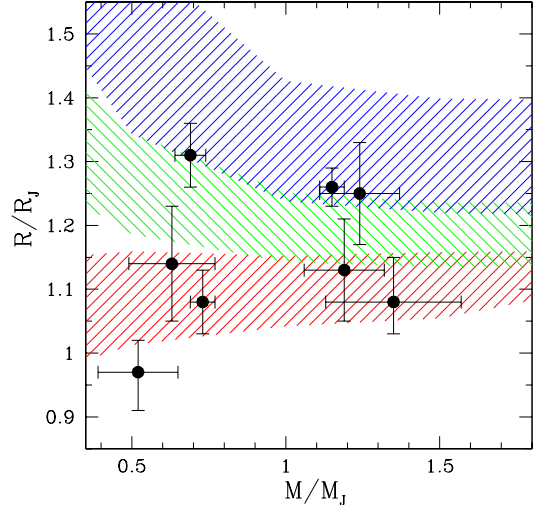

FIG. 15.— Radius vs. mass for observed transiting planets compared to our cooling model. The points with error bars give the observed masses and radii, as listed in Table 1. The lower (red), middle (green), and upper (blue) hatched areas denote $T_{\rm deep} = 500, 2500, 3000$ K. For each $T_{\rm deep}$ and M, the spread in R denotes ages 1 Gyr (top) to 10 Gyr (bottom) in each hatched region. HD 149026's small radius places it well outside the plot.

stant (increasing). The magnitude of δR_1 can be estimated from Figure 12 and eq. (23). Interestingly, R_0 can be somewhat bigger for $M = 0.32 M_J$ than for the higher masses. While a larger radius is expected for strong irradiation, we caution the reader about interpretation of the exact values for R_0. It would be interesting to compare the values obtained by fitting tracks with actual calculations of isothermal planets given a sufficiently accurate low temperature EOS.

Given measurements of planetary mass, radius and age, $T_{\rm deep}$ can be constrained. Figure 14 shows the value of $T_{\rm deep}$ required to explain a planet of a given mass and radius, as represented by different lines, as a function of age. The lines slope up to the right since the cooling must be slower (higher $T_{\rm deep}$) to reach the same radius at larger age. As the lines are not horizontal or vertical, there is significant degeneracy between $T_{\rm deep}$ and age. Large radii in the age range $1 - 10$ Gyr can only be explained by large irradiation temperatures for the mass range $0.32 - 3.2 M_J$. For each mass and radius, there is a minimum age which is set by the unirradiated planet, resulting in a steep slope down to the left. We shall use Figure 14 in § 8 to constrain $T_{\rm deep}$ for the observed transiting planets.

8. APPLICATIONS TO TRANSITING PLANETS

We now compare our theory to the observed masses and radii of the transiting planets (Table 1). Figure 15 shows radius versus mass for the observed transiting planets. The points with errorbars are the data. The three different hatched regions show $T_{\rm deep} = 500, 2500, 3000$ K from bottom to top. The change is gradual from $T_{\rm deep} = 500$ to 2500, and then accelerates for higher temperatures (see Figure 3). Within each hatched region, a spread of ages from 1 (top) to 10 Gyr (bottom) is shown. The radius of HD 149026 is so small as to be well outside the plot. It clearly has a large abundance of heavy elements. The radii of the other

eight planets can be broadly explained with solar composition, ages in the range $1 - 10$ Gyr, and temperatures deep in the atmosphere $T_{\rm deep} \leq 3000$ K. The largest radii requiring the most irradiation are HD 209458, HD 189733 and OGLE-TR-56.

There are significant uncertainties in fitting stars on the main sequence to find stellar ages. Hence there is motivation to understand how a range of ages affects the range of observed radii. Figure 12 shows deviation from the isothermal radius by factors $1.1 - 2$ in the age range $0.1 - 10$ Gyr. The length of each track gives an idea of the uncertainty in radius due to an uncertainty in age. Using the fitting formula in eq. (32), the fractional difference in radius between ages t_1 and t_2 is $\simeq [\eta/(\beta - \delta)](\delta R_1/R_0) \ln(t_2/t_1)$. For the strongly irradiated case, if we choose characteristic values $\eta/(\beta - \delta) = 0.5$, $\delta R_1/R_0 = 0.5$, and a factor of two error in age $t_2 = 2t_1$, the fractional error in radius is 17%. Hence, the age dependence for strongly irradiated planets is important because (i) the decrease in time is steep, and (ii) strong irradiation increases the size of δR_1 relative to δR_0.

Next, the parameter $T_{\rm deep}$ is crucial for the cooling rate, but is not directly measurable. Here we constrain $T_{\rm deep}$ using measured mass, radius and age. We then compare $T_{\rm deep}$ to the equilibrium temperature.

We interpolate over the age $- T_{\rm deep}$ tracks in Figure 14 for the mass and radii appropriate for each planet (except HD 149026, which we do not discuss). Since the uncertainty in $T_{\rm deep}$ due to the error bar in planet mass is smaller than that due to the error bar in radius, we fix the planet mass at the central value and only vary the radius. For those planets with an age range quoted in the literature, we show the age range in the plot, and derive the range of $T_{\rm deep}$ consistent with the age range. These values are listed in Table 1. For those planets with no
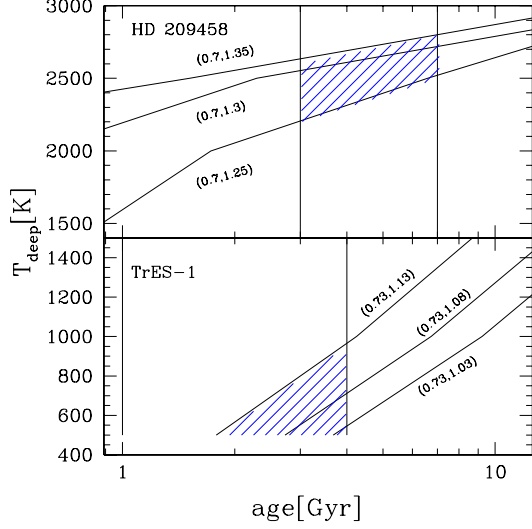
FIG. 16.— Constraints on $T_{\rm deep}$ for HD 209458 and TrES-1. Lines labeled by $(M/M_J, R/R_J)$ given allowed values of $T_{\rm deep}$ versus age for the central value of mass, and a range of radii given by the radius error bar. Vertical lines give age range from main sequence fitting of parent star. Shaded region shows range of $T_{\rm deep}$ allowed given uncertainties in mass, radius and age.
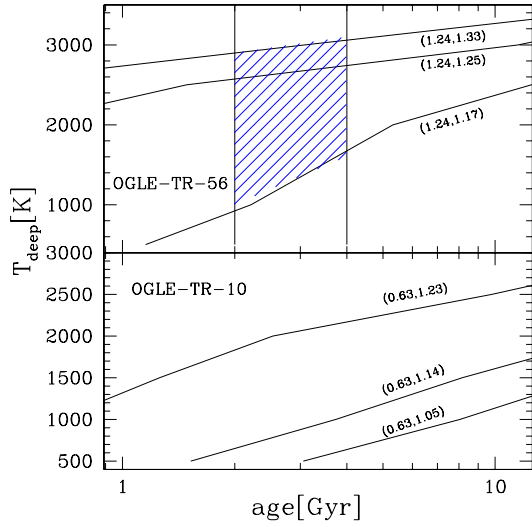

FIG. 17.— Constraints on $T_{\rm deep}$ for OGLE-TR-56 and OGLE-TR-10. See Figure 16 for description.

FIG. 18.— Constraints on $T_{\rm deep}$ for OGLE-TR-111 and OGLE-TR-113. See Figure 16 for description.
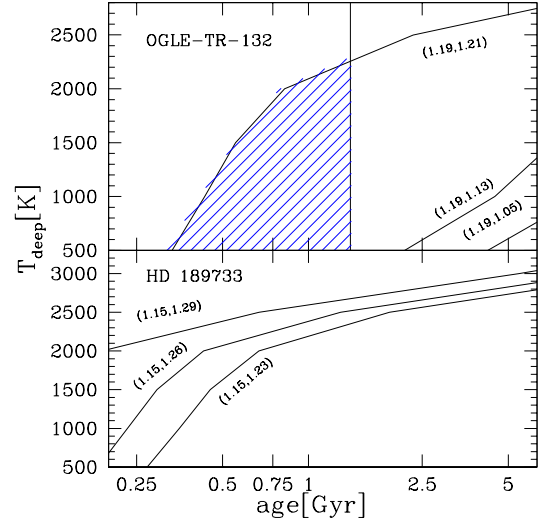
FIG. 19.— Constraints on $T_{\rm deep}$ for OGLE-TR-132 and HD 189733. See Figure 16 for description.

age determination, we find the maximum value of $T_{\rm deep}$ consistent with an age less than 10 Gyr.

The constraints on $T_{\rm deep}$ for all planets except HD 149026 are shown in Figures 16, 17, 18 and 19, and summarized in Table 1. The $T_{\rm deep}$ of HD 209458 is best constrained due to the small error bar on mass and radius, as well as detailed fitting of the parent star to find the age. From Figure 16 we find $T_{\rm deep} = 2200 - 2800$ K; HD 209458b is not consistent with an un-irradiated planet. OGLE-TR-56 has a weak lower limit on $T_{\rm deep}$ which is far less than the equilibrium temperature. All other planets with age constraints have only upper limits, set by the upper limit on the radius, since the lower limit on the radius is consistent with no irradiation. Plots are provided for those planets with no age constraints at the present time.
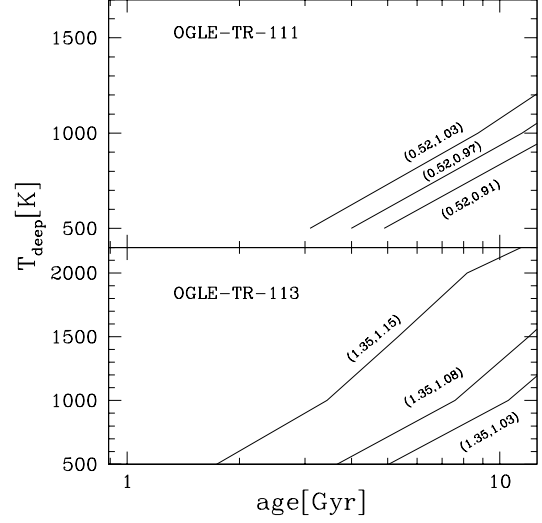
The equilibrium temperature $T_{\rm eq} \equiv T_*(R_*/2a)^{1/2}$ is measurable, but plays no part in our model. On the other hand, the temperature of the deep isotherm is not measurable, but is crucial for the cooling rate. From radiative transfer models, we expect these two temperatures to be roughly proportional, the exact ratio determined by the size of the greenhouse effect (§2). Hence, they should be strongly correlated. Figure 20 shows a plot of $T_{\rm eq}$ versus $T_{\rm deep}$. The large error bars on $T_{\rm deep}$, due to large error bars on the radius, prevent one from drawing robust conclusions. It is in principle possible for a correlation (sloping up to the right) to exist given the current error bars, however, it is not required.

Tighter constraints on $T_{\rm deep}$ require the following:

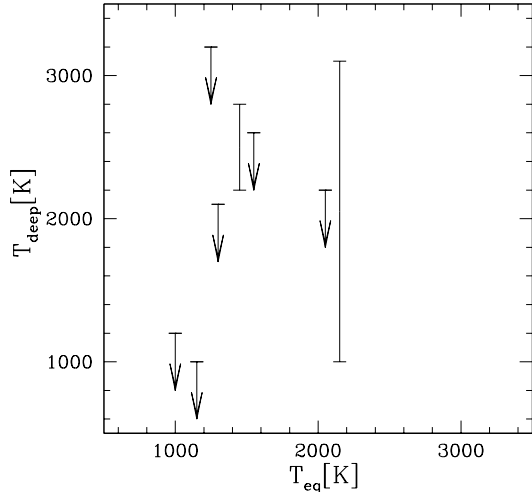- Significantly smaller error bars on the radii of

FIG. 20.— Equilibrium temperature vs. $T_{\rm deep}$. The temperature of the deep isotherm $T_{\rm deep}$ is expected to be strongly correlated with the equilibrium temperature $T_{\rm eq}$, giving a line sloping up to the right. Bracketed lines give constraints on $T_{\rm deep}$, while arrows pointing downward represent upper limits found when no age was available in the literature.

OGLE-TR-56 and OGLE-TR-132.

- An age estimate is needed for HD 189733. If it is found to have an age ≥ 1 Gyr, $T_{\rm deep}$ will be well constrained with a value much larger than $T_{\rm eq}$, similar to HD 209458b.

- Age estimates are needed for OGLE-TR-10, OGLE-TR-111, and OGLE-TR-113. However, given the present error bar on radii of OGLE-TR-10 and OGLE-TR-113, $T_{\rm deep}$ will be constrained only at the factor of two level. OGLE-TR-111 is an interesting case, as it must be older than $\sim 3-4$ Gyr to be consistent with our model.

We encourage efforts in these directions.

9. CONCLUSIONS

We have presented calculations of cooling and radius evolution for strongly irradiated planets. Novel aspects of this model are the following:

- We argue that the generic outcome of strong surface heating, whether it be due to absorption of stellar flux or dissipation of winds and tidal flow, is that a deep isothermal region exists above the radiative-convective boundary. The thermal time in this layer is sufficiently long that the temperature profile is approximately spherically symmetric, irrespective of the size of the asymmetry near the photosphere. We assign this region the temperature $T_{\rm deep}$ and treat it as a boundary condition for the cooling models.

- We show that the cooling flux is determined at the radiative-convective boundary, which is much deeper than the photosphere. Scalings of the flux with core entropy, $T_{\rm deep}$, and mass are computed.

- These scalings allow us to derive an analytic model for the cooling, which shows power-law decrease over a large range of parameter space. The part of the radius which changes in time (the deviation from the isothermal planet) is also a power-law. An analytic formula for radius evolution is given in eq. (32), with coefficients in Table 2.

- While we have used the SCVH EOS and Allard et.al.(2001) opacities for numerical estimates, the analytic solution makes it particularly clear which quantities need to be evaluated for a given opacity table and EOS. The luminosity is sensitive only to the local conditions at the radiative-convective boundary, while the core temperature involves building static (i.e. not time-dependent) models.

We have compared our theory to observed masses and radii for the transiting planets in Table 1 (except for HD 149026, which clearly has a large abundance of heavy elements). Our findings are as follows:

- Figure 15 shows mass versus radius for eight transiting planets, compared to our model. The radii can be broadly explained with solar composition, ages in the range $1-10$ Gyr, and temperatures deep in the atmosphere $T_{\rm deep} \leq 3000$ K. The largest radii requiring the most irradiation to explain are HD 209458, HD 189733 and OGLE-TR-56.

- Figures 16, 17, 18 and 19 show constraints on $T_{\rm deep}$ using measured masses, radii, and ages (when available), and their uncertainties. We find that only HD 209458b is well constrained, with $T_{\rm deep} = 2200 - 2800$ K. OGLE-TR-56 has a weak lower limit, and the other six planets have only upper limits, due to the large measurement uncertainty in the radius, or lack of an age determination. These constraints are summarized in Table 1.

- The equilibrium temperature $T_{\rm eq}$ is measurable, but plays no part in our model. The deep isothermal temperature $T_{\rm deep}$ is not measurable, but is crucial for the cooling rate. Radiative transfer calculations find these two temperatures should be strongly correlated. Figure 20 shows $T_{\rm eq}$ versus $T_{\rm deep}$. As only upper limits on $T_{\rm deep}$ are available for all but HD 209458b and OGLE-TR-56, it is difficult to draw conclusions at the present time. It is in principle possible for a correlation to exist given the current error bars, however, it is not required.

We hope that our models have illuminated the need for more accurate ages and radii. Once those are in hand, our calculations will provide a measurement of $T_{\rm deep}$ of adequate accuracy to compare to $T_{\rm eq}$, thus constraining greenhouse physics and day-night transport.

REFERENCES

Allard, F., Hauschildt, P. H., Alexander, D. R., Tamanai, A., & Schweitzer, A. 2001, ApJ, 556, 357

Baraffe, I., Chabrier, G., Barman, T. S., Allard, F., & Hauschildt, P. H. 2003, A&A, 402, 701

Baraffe, I., Selsis, F., Chabrier, G., Barman, T. S., Allard, F., Hauschildt, P. H., & Lammer, H. 2004, A&A, 419, L13

Baraffe, I., Chabrier, G., Barman, T. S., Selsis, F., Allard, F., & Hauschildt, P. H. 2005, A&A, 436, L47

Barman, T. S., Hauschildt, P. H., & Allard, F. 2001, ApJ, 556, 885

Bildsten, L., Brown, E. F., Matzner, C. D., & Ushomirsky, G. 1997, ApJ, 482, 442

Bodenheimer, P., Lin, D. N. C., & Mardling, R. A. 2001, ApJ, 548, 466

Bodenheimer, P., Laughlin, G., & Lin, D. N. C. 2003, ApJ, 592, 555

Bouchy, F., Pont, F., Santos, N. C., Melo, C., Mayor, M., Queloz, D., & Udry, S. 2004, A&A, 421, L13

Bouchy, F., et al. 2005, ArXiv Astrophysics e-prints, arXiv:astro-ph/0510119

Burkert, A., Lin, D. N. C., Bodenheimer, P. H., Jones, C. A., & Yorke, H. W. 2005, ApJ, 618, 512

Burrows, A., Hubeny, I., & Sudarsky, D. 2005, ApJ, 625, L135

Burrows, A. 2005, Nature, 433, 261

Burrows, A., Guillot, T., Hubbard, W. B., Marley, M. S., Saumon, D., Lunine, J. I., & Sudarsky, D. 2000, ApJ, 534, L97

Burrows, A., Hubeny, I., Hubbard, W. B., Sudarsky, D., & Fortney, J. J. 2004, ApJ, 610, L53

Burrows, A., Sudarsky, D., & Hubbard, W. B. 2003, ApJ, 594, 545

Charbonneau, D., Brown, T. M., Latham, D. W., & Mayor, M. 2000, ApJ, 529, L45

Charbonneau, D., Brown, T. M., Noyes, R. W., & Gilliland, R. L. 2002, ApJ, 568, 377

Charbonneau, D., et al. 2005, ApJ, 626, 523

Cho, J. Y.-K., Menou, K., Hansen, B. M. S., & Seager, S. 2003, ApJ, 587, L117

Chabrier, G., Barman, T., Baraffe, I., Allard, F., & Hauschildt, P. H. 2004, ApJ, 603, L53

Clayton, D. D. 1983, "Principles of stellar evolution and nucleosynthesis", Chicago:

Cody, A. M., & Sasselov, D. D. 2002, ApJ, 569, 451

Cooper, C. S., & Showman, A. P. 2005, ApJ, 629, L45

Deming, D., Seager, S., Richardson, L. J., & Harrington, J. 2005, Nature, 434, 740

Fortney, J. J., & Hubbard, W. B. 2004, ApJ, 608, 1039

Fortney, J. J., Sudarsky, D., Hubeny, I., Cooper, C. S., Hubbard, W. B., Burrows, A., & Lunine, J. I. 2003, ApJ, 589, 615

Goldreich, P., & Nicholson, P. D. 1977, Icarus, 30, 301

Guillot, T., Gautier, D., Chabrier, G., & Mosser, B. 1994, Icarus, 112, 337

Guillot, T., Burrows, A., Hubbard, W. B., Lunine, J. I., & Saumon, D. 1996, ApJ, 459, L35

Guillot, T., & Showman, A. P. 2002, A&A, 385, 156

Saumon, D., & Guillot, T. 2004, ApJ, 609, 1170

Hubbard, W. B. 1977, Icarus, 30, 305

Hubbard, W. B., Burrows, A., & Lunine, J. I. 2002, ARA&A, 40, 103

Hubbard, W. B., Fortney, J. J., Lunine, J. I., Burrows, A., Sudarsky, D., & Pinto, P. 2001, ApJ, 560, 413

Hubeny, I., Burrows, A., & Sudarsky, D. 2003, ApJ, 594, 1011

Iro, N., Bézard, B., & Guillot, T. 2005, A&A, 436, 719

Landau, L. D., & Lifshitz, E. M. 1959, Course of theoretical physics, Oxford: Pergamon Press, 1959,

Lubow, S. H., Tout, C. A., & Livio, M. 1997, ApJ, 484, 866

Marcy, G. W., & Butler, R. P. 1995, Bulletin of the American Astronomical Society, 27, 1379

Marcy, G. W., Butler, R. P., Williams, E., Bildsten, L., Graham, J. R., Ghez, A. M., & Jernigan, J. G. 1997, ApJ, 481, 926

Mayor, M., & Queloz, D. 1995, Nature, 378, 355

Menou, K., Cho, J. Y.-K., Seager, S., & Hansen, B. M. S. 2003, ApJ, 587, L113

Moutou, C., Pont, F., Bouchy, F., & Mayor, M. 2004, A&A, 424, L31

Laughlin, G., Wolf, A., Vanmunster, T., Bodenheimer, P., Fischer, D., Marcy, G., Butler, P., & Vogt, S. 2005, ApJ, 621, 1072

Konacki, M., Torres, G., Sasselov, D. D., & Jha, S. 2005, ApJ, 624, 372

Ogilvie, G. I., & Lin, D. N. C. 2004, ApJ, 610, 477

Pont, F., Bouchy, F., Queloz, D., Santos, N. C., Melo, C., Mayor, M., & Udry, S. 2004, A&A, 426, L15

Potekhin, A. Y., & Chabrier, G. 2000, Phys. Rev. E, 62, 8554

Santos, N. C., et al. 2006, ArXiv Astrophysics e-prints, arXiv:astro-ph/0601024

Sasselov, D. D. 2003, ApJ, 596, 1327

Sato, B., et al. 2005, ApJ, 633, 465

Saumon, D., Chabrier, G., & van Horn, H. M. 1995, ApJS, 99, 713

Saumon, D., Chabrier, G., Wagner, D. J., & Xie, X. 1999, ArXiv Astrophysics e-prints, arXiv:astro-ph/9909168

Saumon, D., Hubbard, W. B., Burrows, A., Guillot, T., Lunine, J. I., & Chabrier, G. 1996, ApJ, 460, 993

Showman, A. P., & Guillot, T. 2002, A&A, 385, 166

Sozzetti, A., et al. 2004, ApJ, 616, L167

Sudarsky, D., Burrows, A., & Pinto, P. 2000, ApJ, 538, 885

Torres, G., Konacki, M., Sasselov, D. D., & Jha, S. 2004, ApJ, 609, 1071

Vidal-Madjar, A., Lecavelier des Etangs, A., Désert, J.-M., Ballester, G. E., Ferlet, R., Hébrard, G., & Mayor, M. 2003, Nature, 422, 143

Vidal-Madjar, A., et al. 2004, ApJ, 604, L69

Wu, Y. 2004, ArXiv Astrophysics e-prints, arXiv:astro-ph/0407628

Zapolsky, H. S., & Salpeter, E. E. 1969, ApJ, 158, 809